Accepted manuscript for publication at Atmospheric Environment – please see final version at https://doi.org/10.1016/j.atmosenv.2020.118037

Analysis of two heat wave driven ozone episodes in Barcelona and surrounding region: Meteorological and photochemical modeling

Clara Jaén, Mireia Udina *, Joan Bech

Departament de Física Aplicada – Meteorologia, Universitat de Barcelona, C/ Martí i, Franquès, 1, 08028 Barcelona, Spain

A B S T R A C T

During the summer of 2019 unusual exceedances of ozone concentration affected NE Spain. A detailed study of two heat wave driven ozone episodes is presented based on the high resolution forecast air quality ARAMIS system, which integrates WRF and CMAQ models. The events occurred on June 28–29 and July 23 2019 and were characterized by synoptic anticyclonic conditions, surface temperatures over the 98th percentile (over the last 40 years), and high ozone values recorded inland due to precursors advection (NO_x and VOCs) mainly from Barcelona Metropolitan Area (AMB), limited by an eastern and a western valley. The analysis of measured and ARAMIS modeled concentrations showed that advection on June 28 and July 23 made its way through the eastern Barcelona valley and on June 29 through the western one. Ozone concentration forecasts reflect a general tendency to overestimate peaks, underestimate in low concentration areas and to increase ozone concentrations earlier than observed. Additionally, a trajectory analysis confirmed the precursor advection from AMB and the recirculation between June 28 and June 29. Finally, NO_2 measured in Barcelona was found to have influence in urban and rural ozone concentrations (100 km from AMB).

1. Introduction

Tropospheric ozone is a secondary atmospheric pollutant with strong oxidizing properties and important effects upon human health, vegetation and materials (Anenberg et al., 2010; Arnold et al., 2018). Ozone concentrations depend on local formation and background but also in long-range and regional transport. Ozone formation is strongly affected by the presence of solar radiation and precursors such as NO_x ($NO + NO_2$), CH_4, CO and volatile organic compounds (VOCs) (Chameides and Walker, 1973; Crutzen, 1973). Photolysis of NO_2 usually

initiates ozone formation and its destruction may be inhibited by the presence of other precursors leading to high ozone accumulations.

Formation sensibility to both main precursors (NO_x and VOCs) is still under laboratory and modeling investigation (Sillman et al., 1990; Sillman and He, 2002; Wei et al., 2019b; Yu et al., 2020; Souri et al., 2020). These studies evaluate chemical factors that regulate two different regimes: NO_x-limited and VOCs-limited. Under high VOCs/NO_x ratios, ozone is more sensitive on NO_x, increasing its concentration if NO_x does. This NO_x-sensitive regime is more common in suburban and rural areas situated downwind from emission sources. On the other hand, under low VOCs/NO_x ratios, increasing NO_x may reduce O_3. This VOCs-limited regime takes place in urban areas which can actually register higher ozone concentrations on non-working days due to road traffic reduction. This phenomena is known as ''weekend effect'' or ''holiday effect'' (Heuss et al., 2003; Qin et al., 2004; Chen et al., 2019; Elansky et al., 2020).

Strong solar radiation ($\lambda > 424$ nm) is needed for initial photolysis and temperature and humidity also influence ozone production. Therefore, ozone concentrations are highly variable along the year and time of day, usually being maximum at summer day afternoons. The nonlinear temperature and humidity relations with ozone production have been previously described by several studies (Stathopoulou et al., 2008; Camalier et al., 2007; Pusede et al., 2015; Wei et al., 2019a; Gu et al., 2020). Generally, increasing temperature and decreasing relative humidity lead to an increase of tropospheric ozone levels. However, different behaviors are described depending on the urbanization and characteristics of the region. Pusede et al. (2015) analyzed several chemical variables involved in ozone-temperature relationships including the organic reactivity with radicals in the atmosphere, the HO_x production and NO_x lifetime. All of them present temperature dependence as a function of O_3 precursor abundance and composition.

In heat wave conditions, stagnant synoptic patterns lead to high temperatures and low wind speeds, which favor ozone accumulation and pose a risk to human health. Hence, usually extreme ozone events have been related with extreme temperatures and high mortality all around the globe (Williams et al., 2012; Pu et al., 2017; Schnell and Prather, 2017; Pyrgou et al., 2018; Zhao et al., 2019; Gu et al., 2020). Consequently, in a climate change scenario, global warming projects increasing heat waves occurrence and intensity, and also increasing ozone related to them if no mitigation in precursor emissions is applied (Meehl et al., 2018). Jacob and Winner (2009) expects a rise in ozone production in polluted areas whereas ozone background levels are expected to be reduced due to higher water vapor concentrations. Globally, integrated model simulations show a decrease of tropospheric ozone burden and lifetime (Stevenson et al., 2005; Racherla and Adams, 2006). However, some local modeling studies expect increasing ozone despite the mitigation strategies applied (Colette et al., 2015) and a higher ozone-related mortality (Lee et al., 2017). Another factor to consider here is the so-called ozone-suppression effect (Steiner et al., 2010) which implies that for air temperatures above 39 °C, due to biophysical and chemical feedbacks, ozone concentration does not necessarily increase with temperature and it may even decrease which has led to review climate projection studies upon ozone extremes (Shen et al., 2016).

Studies over the western Mediterranean basin reported several local characteristics of O_3 dynamics (Millán et al., 1996, 1997, 2000; Querol et al., 1998, 2017; Gangoiti et al., 2001; Carnerero et al., 2019; Massagué et al., 2019). In particular, coastal recirculations driven by sea breezes which consist in daytime cool air flowing inland at surface levels, play a key role in pollutant dynamics. The sea breeze front is characterized by upward currents which return seaward aloft, and usually widespread sinking occurs over the sea to close circulation. Seaward flows aloft followed by night seaward wind flows can create pollutant layers at different elevations over the sea. These layers sink during day-time leaving ozone reservoirs at low levels that can be advected back to the land when breezes onset. This mechanism can exist during several consecutive days depending on the synoptic meteorological conditions. In this scenario, high insolation conditions enhance photochemical transformations of accumulated pollutants into oxidants. Another characteristic mechanism observed is O_3 fumigation. It occurs during the morning growth of the mixed layer which introduces previous days O_3 from the residual layer (stored aloft during night-time) and contributes to rise surface ozone concentrations. This process may be enhanced by vertical diffusion favored by the presence of a Low Level Jet (LLJ) - see Corsmeier et al. (1997), Hu et al. (2013) and Udina et al. (2020). Moreover, regional transport from Central Europe also plays a relevant role in Southern Europe coastal areas such as the region of study of this paper.

Air quality modeling including the Weather Research and Forecasting (WRF) meteorological model and the Community Multiscale Air Quality modeling system (CMAQ) photochemical model are used to study the ozone episodes. This modeling system has been widely used at regional scales around the world. In addition, process analysis of CMAQ is often computed to quantify each individual chemical and physical process that contributes to the pollutant concentration changes (e.g. Gonçalves et al. (2009), Liu et al. (2010), Li et al. (2012), Zhang et al. (2019) and Udina et al. (2020)).

Ozone episodes occur when ground-level concentrations exceed threshold values set by legislation and may have a great impact to human health. North from Barcelona metropolitan area, air quality standards are sometimes exceeded and tropospheric ozone is usually under special surveillance. The objective of this study is to characterize two ozone episodes that took place in this region during the summer of 2019. A detailed study of the influencing meteorological factors, the areas affected, the consequences and the capacity to forecast the events is presented.

Section 2 describes the study area, its local ozone measurement network, legislation and the modeling strategy used. Results presented are organized in Sections 3 and 4. Firstly, a general view of ozone situation in Catalonia over the years and the particularities of 2019 heat waves; and secondly, an specific study of two ozone episodes which occurred in 2019. Characterization includes the analysis of measurement data, model simulation verification, spatial distribution, dominant processes, trajectories and NO_2-ozone relation. Finally, conclusions are exposed in Section 5.

2. Methodology

2.1. Study area

This study is focused on Barcelona, capital of Catalonia, and surrounding area (NE Spain) (Fig. 1) characterized by complex topography. It is situated within the temperate zone of the northern hemisphere, in south-west Europe, under the influence of the Mediterranean Sea. Although summer season is predominantly dry (Mediterranean climate), the variety of Catalan geography makes the territory present a great climate diversity.

Most of the population and industrial areas are located on the coast, mainly in or near Barcelona. The high industrial activity and road and shipping transport emissions in the Barcelona Metropolitan Area (AMB) compose the most important source of NO_x and VOCs in the Catalan territory. Sometimes high pollutant concentrations are observed inland due to sea-breeze advection of pollutants capable of transporting air masses from the coast to the rural territory inland. Several valleys crossing the coastal Catalan ranges favor pollutant transport from AMB to inland cities. Sea breezes structure in the area and, consequently their contribution to pollutant transport, are mainly driven by the topography and synoptic flow. Sea breezes flow combined with upslope wind contribute to vertical transport, whilst horizontal dispersion is limited by topography (Soler et al., 2011). Hence, transport of anthropogenic emissions of NO_x and VOCs combined with biogenic VOCs and high insolation may cause severe ozone episodes in inland settled areas (Toll and Baldasano, 2000; Valverde et al., 2016; Massagué et al., 2019).

2.2. Local legislation and measurement network

Catalonia is covered by a ground level measurement station network, the *Xarxa de Vigilància i Previsió de la Contaminació Atmosfèrica* (XVPCA) which includes 75 automatic stations classified according to local emissions (background, industrial or traffic) and land use (rural, suburban or urban). Ozone is measured at 49 XVPCA stations. Local authorities define and set Air Quality Goals (AQG) following the reference legislation which in case of ozone are the following:

- **ITE** (Information Threshold Exceedance): hourly-mean values > 180 μg/m^3.
- **ATE** (Alert Threshold Exceedance): hourly-mean values > 240 μg/m^3.
- **HHPV** (Human Health Protection Value): 8 h moving average day maximum > 120 μg/m^3.

The World Health Organization also base their thresholds in 8 h averages. It sets the Air Quality Guideline in 100 μg/m^3 which provides adequate protection of public health and also defines the Interim target-1 (160 μg/m^3) and High levels (240 μg/m^3) with important and significant health effects, respectively (WHO, 2006).

2.3. Modeling strategy

Pollutant species concentrations (O_3 and NO_2) are modeled with the high resolution air quality modeling system ''A Regional Air Quality Modeling Integrated System'' (ARAMIS) developed by the Mesoscale and Microscale Atmospheric Modeling and Research group (MAiR) from the University of Barcelona (Soler et al., 2015). It integrates three coupled Eulerian models: a meteorological, an emission and a photochemical model. On the other hand, air parcel trajectories are calculated in order to estimate the origin of the air masses in the episodes.

2.3.1. Air quality modeling

Meteorological model fields are simulated with the Weather Research and Forecasting model (WRF-ARW) version 3.5 (Skamarock et al., 2008). It is a fully-compressible non-hydrostatic model with terrain following vertical coordinates and a horizontal and vertical Arakawa C-grid type. It is configured using three one-way nested domains with horizontal resolutions of 27 km (D1), 9 km (D2) and 3 km (D3). The last domain covers our area of interest, the entire region of Catalonia (Fig. 1). Initial and boundary conditions are taken from the European Center for Medium-Range Weather Forecast global model (ECMWF) with a 0.5° x 0.5° resolution, and the boundary conditions are forced every 6 h. In the vertical, the model includes 32 levels in all domains, with 20 levels below approximately 1500 m and the first level at 15 m. The WRF physics package employed includes the Eta surface layer scheme, which is based on Monin–Obukhov similarity theory (Monin and Obukhov, 1954), the YSU boundary layer scheme (Hong et al., 2006), the rapid radiative transfer model (RRTM) for longwave radiation (Mlawer et al., 1997), the Dudhia parametrization for shortwave radiation (Dudhia, 1989), the New Thompson microphysics parametrization (Thompson et al., 2004), the Grell three-dimensional cumulus parametrization (Grell and Dévényi, 2002) and the Noah land-surface parametrization (Chen and Dudhia, 2001). Simulations are run for 72 h, taking the first 24 h as spin-up time to minimize the effects of initial conditions.

The High Resolution Emission Model (HIREM) (Ortega et al., 2009; Arasa et al., 2012; Soler et al., 2015) includes the emissions from natural and anthropogenic sources classifying the primary pollutants in nitrogen oxide (NO_x), methane (CH_4) and non-methane volatile organic compounds (NMVOC), carbon monoxide (CO), carbon dioxide (CO_2), nitrous oxide (N_2O), sulfur dioxide (SO_2), total suspended particles (TSP) and particulate matter (PM_{10} and $PM_{2.5}$). For the larger domains D1 and D2 a top-down methodology is used to disaggregate the EMEP/CORINAIR emissions of 2013. For the small domain D3 a bottom-up technique is used, including the local information of industrial inventories, road traffic emission calculation and biogenic natural emissions, revised in depth in 2011 and with further minor updates.

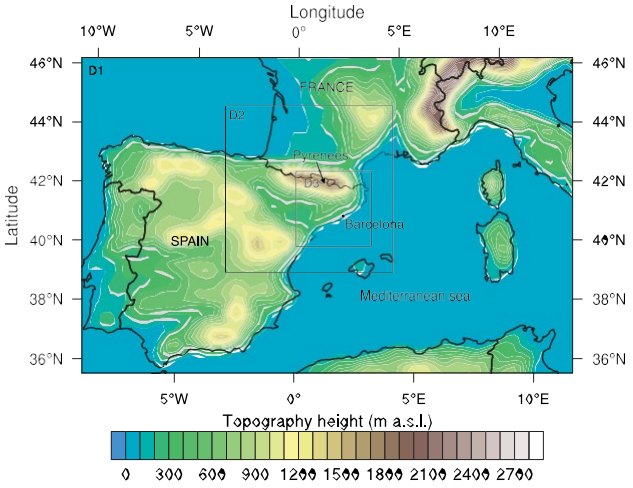

Fig. 1. Topography and modeling domains of ARAMIS system: D1, D2 and D3, using 27, 9 and 3 km horizontal grid sizes respectively. (For interpretation of the references to color in this figure legend, the reader is referred to the web version of this article.)

The photochemical model is the Community Multiscale Air Quality Modeling System (CMAQ), version 5.1 (Byun et al., 1999). For the simulation of chemical mechanisms, we used the Carbon Bond (CB05) and the associated Euler Backward Solver (EBI) (Yarwood et al., 2005) including gas-phase reactions involving nitrogen pentoxide (N_2O_5) and water (H_2O); this solver removes obsolete chemical combinations in gas, aerosol (solid or liquid) and aqueous phases. In addition, we used the aerosol module AERO4 with preliminary treatment of sea-salt emissions and chemistry. To treat clouds in the model, we used the ACM boundary-layer parametrization (Pleim and Chang, 1992). Boundary conditions and initial values for domain D1 came from a vertical profile supplied by CMAQ itself, whilst boundary and initial conditions for domains D2 and D3 were supplied by domain D1 and D2, respectively. As in the meteorological model, CMAQ provides 72 h forecasts, taking the first 24 h as spin-up time to minimize the effects of initial conditions. It should be noted that modeled values represent instantaneous concentrations while observed records are hourly averaged concentrations. MCIP v4.3 is run to ingest meteorological output from WRF to CMAQ model, using 31 vertical layers. In addition, process analysis of CMAQ model is included in order to quantify the physical and chemical processes involved in the calculation of ozone concentrations. In particular, the Integrated Process Rate (IPR) gives information about the individual processes including horizontal and vertical advection, horizontal and vertical diffusion, chemical reactions, cloud processes and dry deposition.

Model verification has been performed with four statistical parameters, namely the Mean Bias (MB) (Eq. (1)), Mean Absolute Error (MAE) (Eq. (2)), Root Mean Square Error (RMSE) (Eq. (3)) and Regression coefficient (R) (Eq. (4)), given by:

$$MB = \frac{1}{n}\sum_{i=1}^{n} m_i - o_i \quad (1)$$

$$MAE = \frac{1}{n}\sum_{i=1}^{n} |m_i - o_i| \quad (2)$$

$$RMSE = \sqrt{\frac{1}{n}\sum_{i=1}^{n} (m_i - o_i)^2} \quad (3)$$

$$R = \frac{\sum_{i=1}^{n}(m_i - \overline{m})(o_i - \overline{o})}{\sum_{i=1}^{n}(m_i - \overline{m})^2} \quad (4)$$

where m_i and o_i are, respectively, the model and the observation values at time i and n is the total number of times.

Moreover, the ozone forecast has been also evaluated for different hourly concentrations with contingency tables in Appendix B.

2.3.2. Modeled trajectories

Air parcel trajectories have been calculated with the Hybrid Single-Particle Lagrangian Integrated Trajectory (HYSPLIT) model developed by the National Oceanic and Atmospheric Administrations (NOAA) (Stein et al., 2015). The model computes simple forward and backward trajectories as well as dispersion, chemical transformations or surface deposition. Calculation is made with an hybrid method between the Lagrangian approach to calculate advection and diffusion whilst the Eulerian method is used for concentration simulations.

Meteorological fields from the D3 WRF-ARW domain (3-km horizontal grid resolution) are used as input for HYSPLIT to analyze simple forward and backward air parcel trajectories affecting XVPCA stations measurements. In order to characterize the advection of precursors, 10 h backward trajectories have been calculated from the receptor stations starting the simulation when high ozone concentrations were registered. In addition, 10 h forward trajectories are computed to study the transport of ozone and its precursors from the affected receptor stations. Both types of trajectories have been initialized at 8 m above ground level where the first level of the model is located.

3. Ozone overview results

The year 2019 had several days with abnormally high hourly ozone values with 115 h of Information Threshold Exceedances (ITEs), 7 h of Alert Threshold Exceedances (ATEs) and 678 daily maximum 8 h moving averages over the HHPV. These high values are very unusual for the last decade even in an area like Catalonia with problematic ozone concentrations. The information and alert threshold incidences normalized by the number of measuring stations since 1991 to 2019 are represented in Fig. 2. An incidence, in this case, is a group of consecutive hours with threshold exceedances during the ozone surveillance campaign. The normalized alert threshold incidences from 1991 to 2019 (Fig. 2) were high between 1991 and 2003 and non-existent from 2007 to 2018 probably due to more emission restrictions set by European and local legislation in the beginning of the twenty-first century. The normalized information threshold incidences show a great variability along the years but also present higher values during the first monitoring years.

The high number of incidences of 2003 (Fig. 2) are temperature-related since most of them took place during an important heat wave which lasted about two weeks. That heat wave affected different European countries and several studies analyzed the ozone temperature dependence, its relation with mortality during this event and the driving mechanisms involved (Dear et al., 2005; Filleul et al., 2006; Lee et al., 2006; Francis et al., 2011). Understanding the meteorology, chemical and transport processes involved in these heat wave driven high ozone concentration episodes is necessary to take action for decreasing human health impact caused by these events. In the present work, we will try to understand the factors influencing the rise in ATEs on 2019, and particularly on heat wave conditions.

Under usual summer meteorological synoptic conditions, the surface level Azores High is located west of the Iberian peninsula and a mid-level tropospheric ridge extends from northern Africa into southern Europe, allowing the development of mesoscale circulations in the area. Local flows are strongly affected by the mesoscale thermal low usually located in western Iberia during this season which implies compensatory subsidence over Mediterranean coasts. A diurnal cycle in wind direction (southerlies during solar hours and northerlies at night) can be observed and, as explained above, these surface winds can produce recirculations of pollutants. This synoptic pattern can coexist with a high pressure located in central Europe. In this situation, Catalonia can be affected by easterly advection of pollutants due to marine surface flows. This easterly advection from Golf of Lion can converge at surface levels with southerly sea breeze leading to cloud covering inland. The combination of these meteorological conditions frequently create suitable environments to ozone production in Catalan territory during summer season. In general, with low pressure gradients under anticyclonic driven situations, flow is controlled by thermal effects so sea breezes have a great development and long-range advection of air masses is not important.

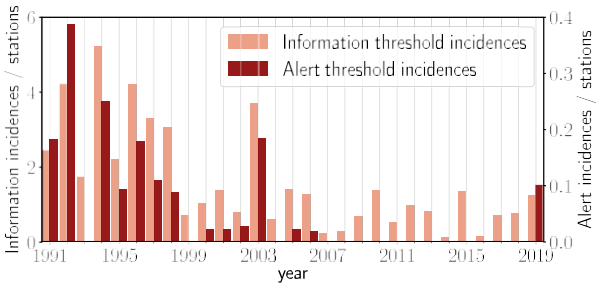

Fig. 2. Normalized ozone alert and information threshold incidences from 1991 to 2019. To account for station network size, normalization is performed by dividing the number of incidences by the number of stations available.

Table 1
Summary of the main characteristics for the studied episodes.

	Episode A		Episode B
Days	June 28	June 29	23 July
ITEs (nº hours)	20 h	49 h	10 h
nº stations with ITEs	8	17	6
ATEs (nº hours)	4 h	1 h	2 h
nº stations with ATEs	3	1	2
Daily maximum 8 h moving average > 120 μg/m³	20	41	13
Daily maximum 8 h moving average > 160 μg/m³	3	12	1
Declared heat waves	25–30 June		22–25 July
Maximum air temperature	43.6 °C	43.8 °C	41.0 °C

Prevailing anticyclonic situations lead to dry summers with high temperatures over the Iberian peninsula. Fig. 3 shows the daily maximum 2 m temperature reanalysis for June, July and August of 2019 compared with data from period 1979–2019. Hourly data was obtained from ECMWF ERA5 reanalysis covering the studied region at surface level and the spatial average was calculated including all cells contained in the area. During the summer of 2019, 98th percentile maximum reanalyzed temperature was exceeded 12 days. Abnormally high temperatures were reached from June 25 to June 30 and from July 22 to July 25. For both periods, heat waves were declared by local authorities recording maximum temperatures of 43.6 °C (June 28), 43.8 °C (June 29), and 41.0 °C (July 23) in stations around Catalan territory. Heat waves are declared by the local administration when, on at least three consecutive days, air temperature observations exceed the 98th percentile of the maximum daily temperature (Meteocat, 2019b,a). Ozone episodes studied in the present work took place during those periods, which illustrates the correlation between high temperature and ozone formation. In fact, 92 ITEs (out of 115 for all summer) occurred during both heat waves.

4. 2019 episodes

In this study, we will focus on the two most intense ozone episodes that took place during the heat waves in summer of 2019. The first

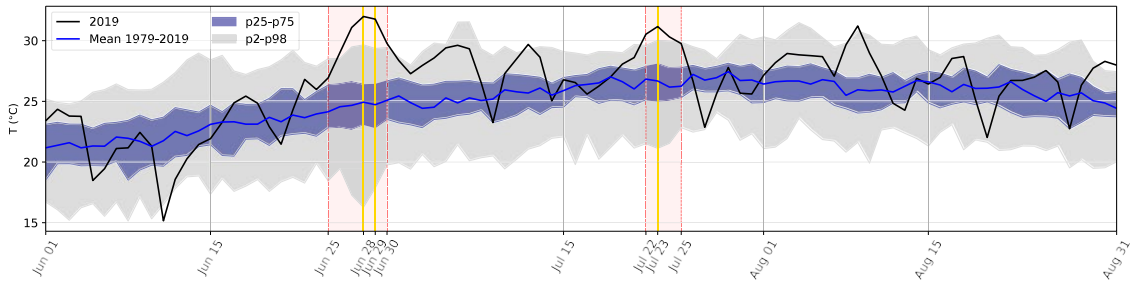

Fig. 3. Daily maximum ERA 5 reanalysis of 2 m temperature in Catalan territory for June, July and August from 1979 to 2019. Dark blue and light gray shaded areas show values from 25th to 75th and from 2th to 98th percentiles, respectively. Red shaded periods correspond to declared heat waves and yellow colored lines correspond to the analyzed episode days (Section 4). (For interpretation of the references to color in this figure legend, the reader is referred to the web version of this article.)

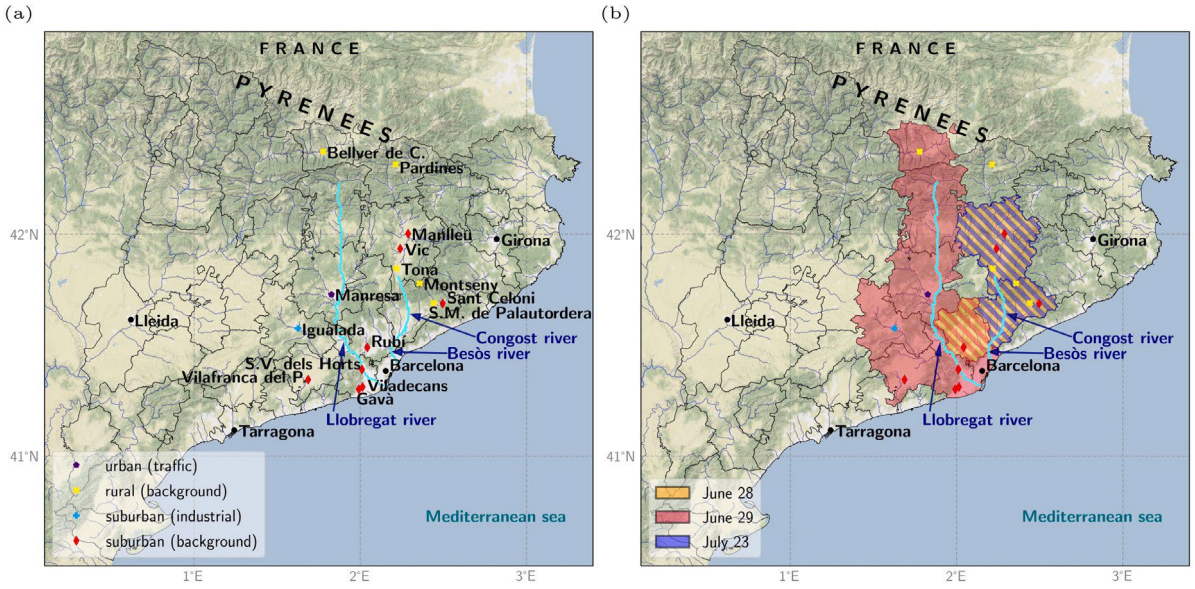

Fig. 4. Region of study with the main geographic features and stations (type and locations) (a). Schematic representation of the most affected regions for both episodes (territory of local counties where exceedances occur) and the rivers pathways (b). (For interpretation of the references to color in this figure legend, the reader is referred to the web version of this article.)

one, Episode A, was a two-day long episode from June 28 to June 29 and Episode B occurred in July 23. Simultaneous characterization will be performed to analyze the causes, consequences, similarities and differences between both episodes. Their main characteristics are summarized in Table 1 including the exceptional number of exceedances during the episodes which disrupt the trends of previous years. Note that for June 29, 41 stations out of 49 registered daily maximum 8 h moving averages over the HHPV and maximum air temperatures were over 40 °C. Also, schematic maps are shown in Fig. 4 which includes the main stations affected and their classification, the river pathways (blue lines), the affected counties for the studied days and also the most important features of the region and selected towns.

Regarding the synoptic scale (Fig. 5) , both episodes are characterized by surface anticyclones situated over the Azores and British Isles or central Europe, a thermal low in central Iberia, and a high pressure ridge at 500 hPa extended from north Africa to most of the Mediterranean basin. For the specific days, midday reanalysis of June 28 displays a relative high over Gulf of Biscay (north of Iberia) which may induce northerlies in the north of Catalonia. For June 29, a cyclonic circulation was placed south of Gulf of Lion (south-east France) leading to strong northerlies in the northern coast of Catalonia. On the other hand, July 23 surface flows are essentially southerlies along the day.

In the north-east part of Catalonia sea breezes have more westward direction due to coast orientation and flow has both regional transport and breeze contributions. The different intensity of both northward and westward sea breeze components will determine the location of the convergence area, therefore, which will be the dominant pollutant advection pathway. Surface winds show that wind convergence over the Catalan territory is located further west for June 29, affecting Llobregat river valley pathway, than for June 28 and July 23, across Besós and Congost rivers valleys. The affected areas are represented in Fig. 4 with different color shades for each day.

4.1. Station measurements

In Episode A the information threshold was exceeded in 25 (out of 49) XVPCA stations while in Episode B only in 4 XVPCA stations. Fig. 6 shows stations with at least one ozone hourly value over 200 μg/m^3. In all cases, ATEs happened between 12 and 14 UTC when solar radiation is more intense and temperatures are typically higher. For both episodes the peak values evolution gives information about surface flow motion. On June 28 (Fig. 6a), the earliest peaks were registered in Rubí and Sant Celoni, stations located relatively close to the high precursor emission source area of Barcelona. As time passed, peak values were observed in stations farther from the coastline: in Montseny and Tona, at 14 UTC, and in Vic and Manlleu, at 15 and 16 UTC respectively, as diurnal breeze penetrated inland through north-eastern valleys of Barcelona (Besòs-Congost pathway).

Fig. 6b shows June 29 ozone time series of stations located in Barcelona and surroundings. For example, concentrations in station BCN (Observatori Fabra) were higher than in nearby stations most

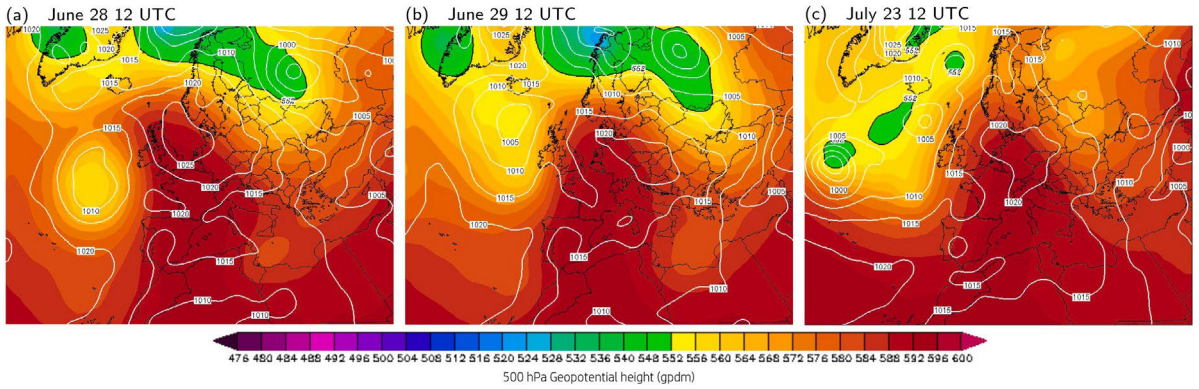

Fig. 5. Sea level pressure (contour lines labeled every 5 hPa) and 500 hPa geopotential height (shaded colors) maps corresponding to June 28 (a), June 29 (b) and July 23 (c) at 12 UTC. Data source: CLIMATE FORECAST SYSTEM reanalysis (CFSR) 0.5° from www.wetterzentrale.de. (For interpretation of the references to color in this figure legend, the reader is referred to the web version of this article.)

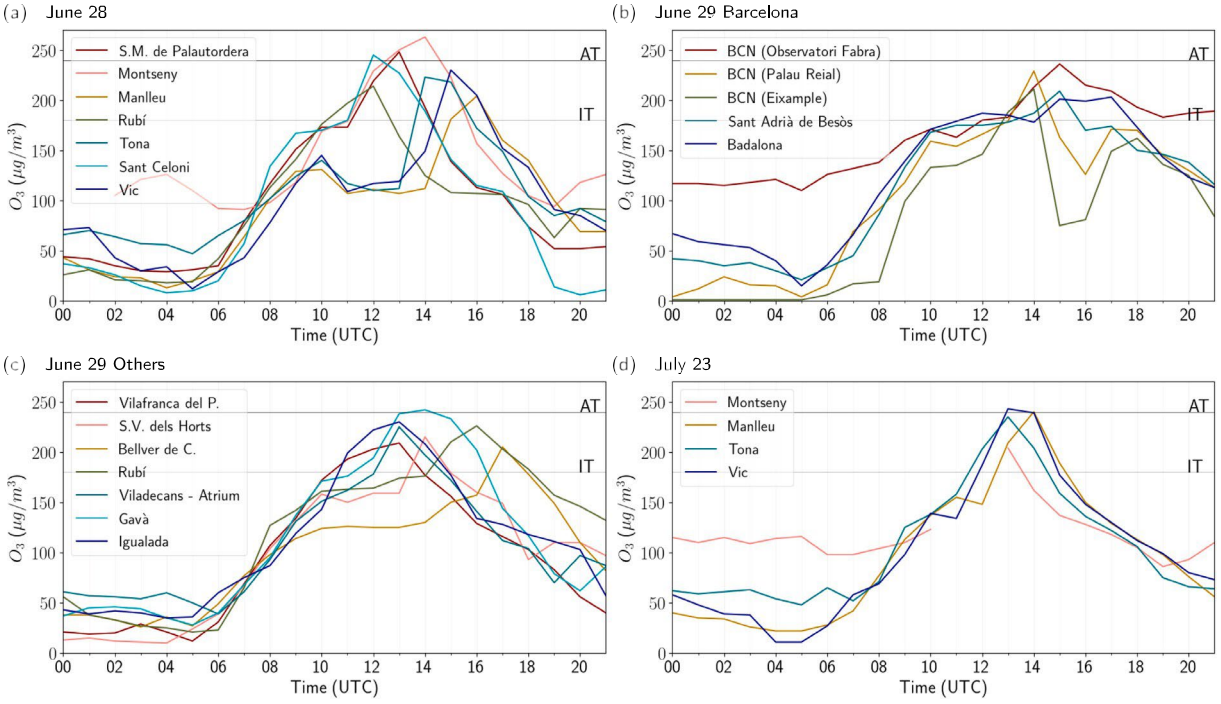

Fig. 6. Time series of O_3 concentration in stations with some hourly value over 200 μg/m³ during both episodes. For all stations during June 28 (a), for the stations located in Barcelona (BCN) and surroundings during June 29 (b), for the stations located outside Barcelona during June 29 (c) and for all stations during July 23 (d). The alert threshold (AT) and the information threshold (IT) are plotted as horizontal gray lines. (For interpretation of the references to color in this figure legend, the reader is referred to the web version of this article.)

part of the day, and particularly high at late afternoon. This station is located at 415 m above sea level which indicates an accumulation of pollutants at that altitude near the coast. For non-Barcelona stations, peak evolution in Fig. 6c shows that sea breeze advected pollutants through western Barcelona Valleys (Llobregat pathway) during that day and high values were recorded even in Bellver de Cerdanya, located in the south side of the Pyrenees, about 100 km away from Barcelona (see Fig. 4). As mentioned above, surface wind convergence determines the dominant pollutant advection pathway affecting different areas both days.

Ozone concentration time series for Episode B are represented in Fig. 6d. Flow evolution follows a similar pattern than in June 28 but fewer stations were affected by high ozone concentrations. As in Episode A, maximum values evolve inland with time. Firstly, the ozone peak is observed in Tona, and afterwards in Vic and Manlleu. In Montseny no values were recorded due to technical problems from 10 to 13 UTC, when other stations observed ozone increases so it seems plausible that during this period concentrations could have been even higher than the first record available at 13 UTC. On June 28 and July 23 exceedances were recorded in this station showing high night concentrations compared to other stations. Montseny station is located at 693 m of altitude compared with 145 m or 460 m of Sant Celoni and Manlleu, respectively. Therefore, Montseny may be measuring background ozone concentrations remaining in high altitudes due to sea breeze recirculation (Soler et al., 2011), similarly to what happened in Episode A during night-time at BCN (Observatori Fabra).

4.2. *Ozone modeling*

4.2.1. *Verification results*

A comparison between modeled and observed ozone concentration time series at selected stations is provided in Fig. 7. In June 28 (Fig. 7a), ARAMIS predicted almost correctly the maximum values reached at station S. M. de Palautordera but a bit earlier than they

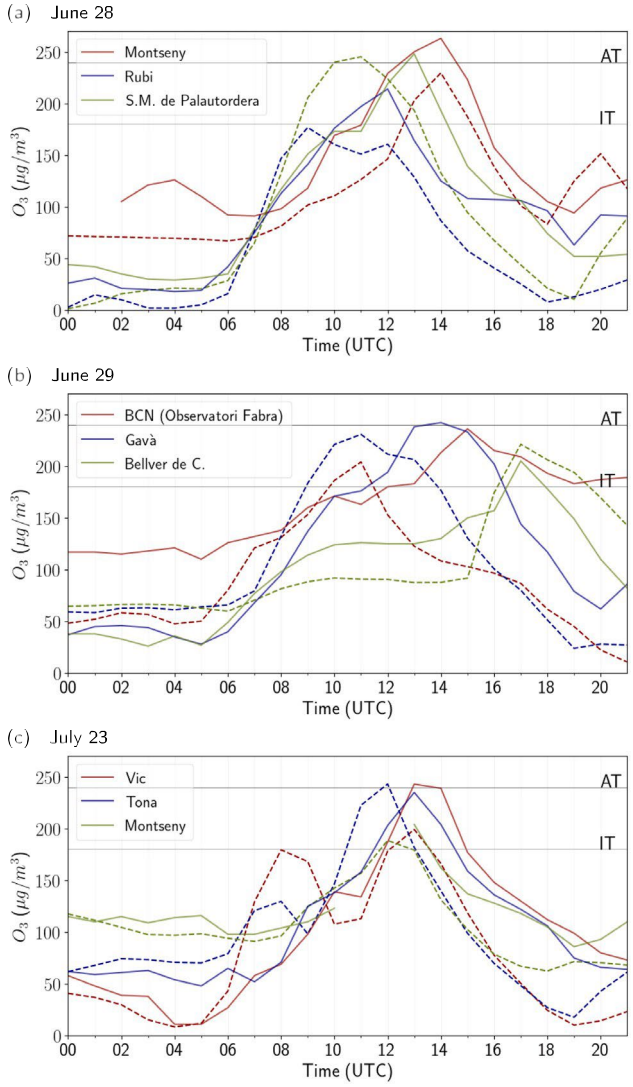

Fig. 7. Modeled (dashed) and measured (solid) time series from representative stations for the episode days. For June 28 in Montseny, Rubí and Santa Maria de Palautordera (a), for June 29 in Observatori Fabra, Gavà and Bellver de Cerdanya (b) and for July 23 in Vic, Tona and Montseny (c). The alert threshold (AT) and the information threshold (IT) are plotted as horizontal gray lines. (For interpretation of the references to color in this figure legend, the reader is referred to the web version of this article.)

were actually measured. This tendency of the model to shift forward in time ozone increases and highs is seen often. In addition, model estimated high values over a larger period of time. However, in the case of Montseny station, both peaks coincide in time but measured time series is always higher than forecasts except at late afternoon. On the other hand, the simulation follows approximately the previously explained elevated night-time ozone concentrations at Montseny. For Rubí station, forecasts reproduce reasonably well the qualitative daily evolution but again the peak is forecast before the observation time and the observed information threshold exceedance is not forecast. Moreover, nocturnal forecasts at this station underestimated observed concentrations, probably because the model is reproducing too much ozone titration in a high NOx emission area.

Modeled ozone for June 29 (Fig. 7b) in BCN (Observatori Fabra) station is considerably lower than measured for almost all day, with highest discrepancies during late afternoon. ARAMIS is not estimating properly night-time ozone at this elevated station. On the contrary, modeled and observed ozone concentrations for Bellver de Cerdanya

Table 2
Ozone concentration model verification statistics for all stations (first row) and for stations exceeding hourly values over 200 μg/m^3 during both episodes (second row).

	MB (μg/m^3)	MAE (μg/m^3)	RMSE (μg/m^3)	R
All stations	−15.8	32.2	41.8	0.652
Stations > 200 μg/m^3	−18.6	42.4	55.5	0.649

are pretty close and, regarding Gavà station, the peak is also estimated earlier.

In July 23 (Fig. 7c) the model simulation reproduces the near-midday peak of Vic in time but it underestimates slightly the ozone concentrations. During morning hours, ARAMIS forecast reaches ITE at this station and a less intense peak in Tona. These peaks are not confirmed by the observations, a situation often repeated in several simulated episodes in Vic surroundings.

Table 2 and Fig. B.1 summarize the model verification of ozone concentrations comparing concurrent observations and model forecasts. Overall, the model underestimates the ozone concentrations in both episodes in a range of 15–19 μg/m^3. Both MAE and RMSE are higher for stations measuring concentrations over 200 μg/m^3 (those shown in Fig. 6), however the correlation coefficient is very similar, around 0.650. Categorical statistics reveal that the forecast is acceptable for concentrations until ~140 μg/m^3 (Fig. B.1), where POD is over FAR. It should be noted that this verification metrics is based on a point-to-point comparison, both in space and time, so it ignores the time lag between high concentrations observed in time series (see Fig. 7) and also slight spatial discrepancies shown in the next section. Therefore, the model provides a reasonably good skill in forecasting ozone concentrations quantified here by the scores described above, which would be even better if more relaxed or fuzzy verification scores were considered (WWRP/WGNE, 2015; Trapero et al., 2013).

4.2.2. Spatial distribution and dominant processes

Model simulations allow us to compare not only point forecasts with observations, but also to explore the spatial field of ozone concentrations and wind patterns in areas where no measurements are available. A selection of comparative maps displaying the most representative features of both episodes is shown in Fig. 8. They include ozone concentration forecasts (shaded colors), observed values (colored circles), wind field forecast (gray arrows) and wind observations at stations of the Meteorological Service of Catalonia (black arrows). In order to highlight the most affected areas, ozone values over alert threshold have been represented in violet tonalities (hourly ozone concentrations > 240 μg/m^3).

As diurnal heat got stronger and breezes onsetted during June 28, a model peak developed on the north-east part of Catalonia (Fig. 8a) due to the advection through Besòs-Congost pathway. As explained above, a number of stations (Sant Celoni, Santa Maria de Palautordera and Montseny) indicated ATE, which were pretty well estimated by ARAMIS (Fig. 8b). Moreover, the model estimated ozone concentrations reaching very high values (about 300 μg/m^3) further in the north-east area where there are no measurement stations or existing ones had technical problems so, unfortunately, these values cannot be verified. In this region, we can also see the easterly flow component entering inland through Gulf of Roses (north-east Catalan coast) which can also contribute to rise O_3 concentrations transporting regional ozone. During the following hours, peak values were displaced northward to Vic surroundings reaching the last maximum in Manlleu at 16 UTC (Fig. 8c). Observed winds confirm advection of AMB pollution to inland stations and the convergence of easterly and southerly flows at onshore regions. As a response of this convergence and the anabatic winds, pollutants were transported upwards and could be distributed towards the sea by breeze aloft. Along night-time, wind blew weakly from a general northerly direction as a result of coupled effect of downslope

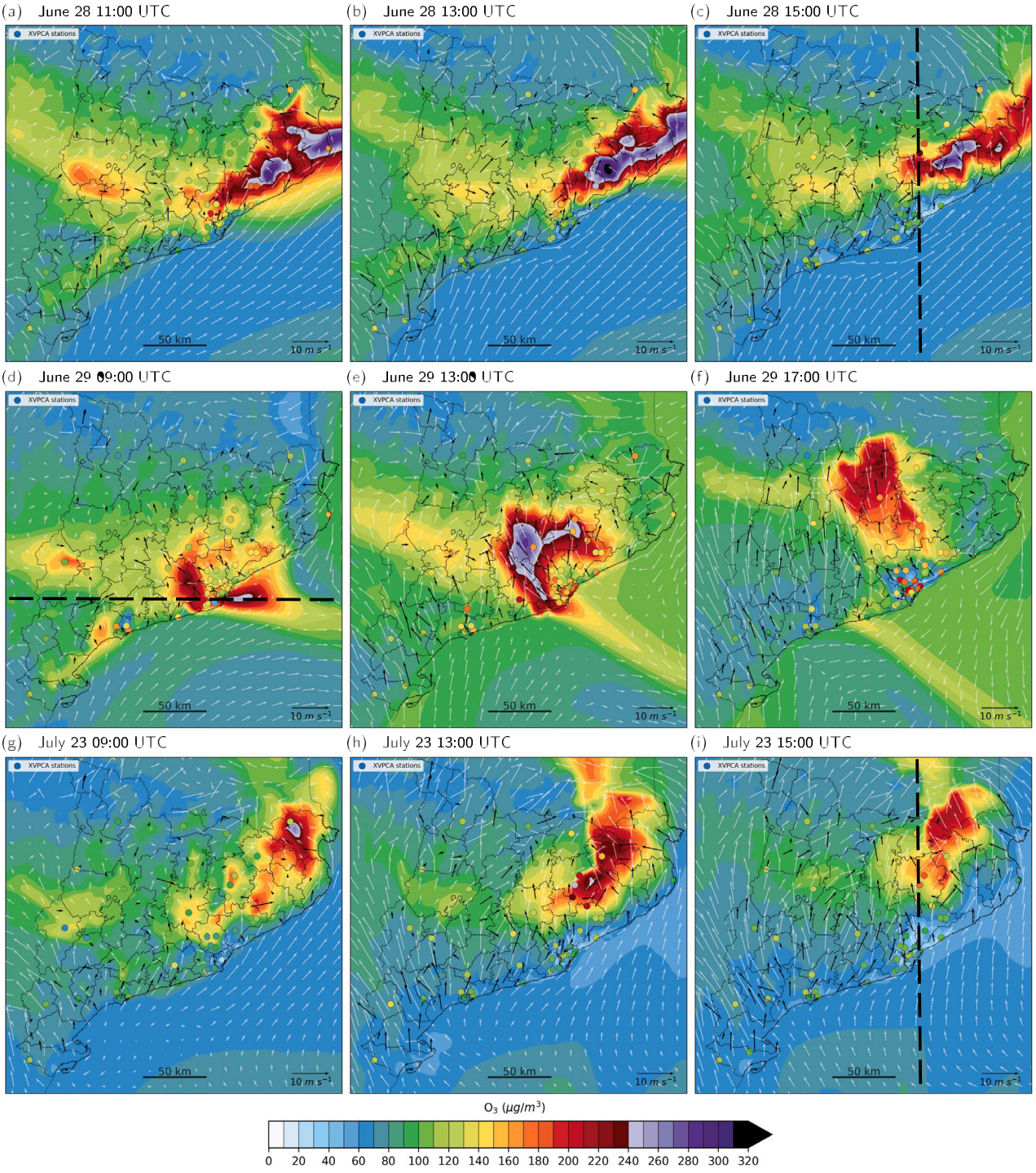

Fig. 8. Ozone concentration forecasts (shaded colors), ozone observations (colored circles), 10-m wind forecasts (white arrows) and 10-m wind observations (black arrows). Maps shown correspond to June 28 at 11:00 UTC (a), June 28 at 13:00 UTC (b), June 28 at 15:00 UTC (c), June 29 at 09:00 UTC (d), June 29 at 13:00 UTC (e), June 29 at 17:00 UTC (f), July 23 09:00 UTC (g), July 23 at 13:00 UTC (h) and July 23 at 15:00 UTC (i). Black dashed lines correspond to cross sections drawn in Figs. 9 and A.1. (For interpretation of the references to color in this figure legend, the reader is referred to the web version of this article.)

night winds and breezes. This airflow may have therefore transported ozone to the coast. Furthermore, model simulations allow to observe the northerlies in the Pyrenees which also contributed to upward pollutant transport and recirculation when converging with breezes (Fig. 9a).

During the morning of June 29 (Fig. 8d) an ozone plume developed in front of Barcelona coast consistent with the aforementioned pollutant recirculation. Ozone and its precursors can be trapped in stacked layers formed along the coast and come back to land the next day (ozone fumigation) (Fig. A.1). Hence, ATE measured in Gavà at 14 UTC may be explained by means of ozone formation via precursors reaction with the morning solar radiation over the sea and the later transport inland combined with ozone recirculation and ozone fumigation from residual layer. The characterization of these dominant processes are further explained at the end of this section. In addition, the main wind component at the port of Barcelona was found to be westward, towards Gavà and Llobregat valley, following an unusual direction. This implied not only advection from air sea layers but also from all

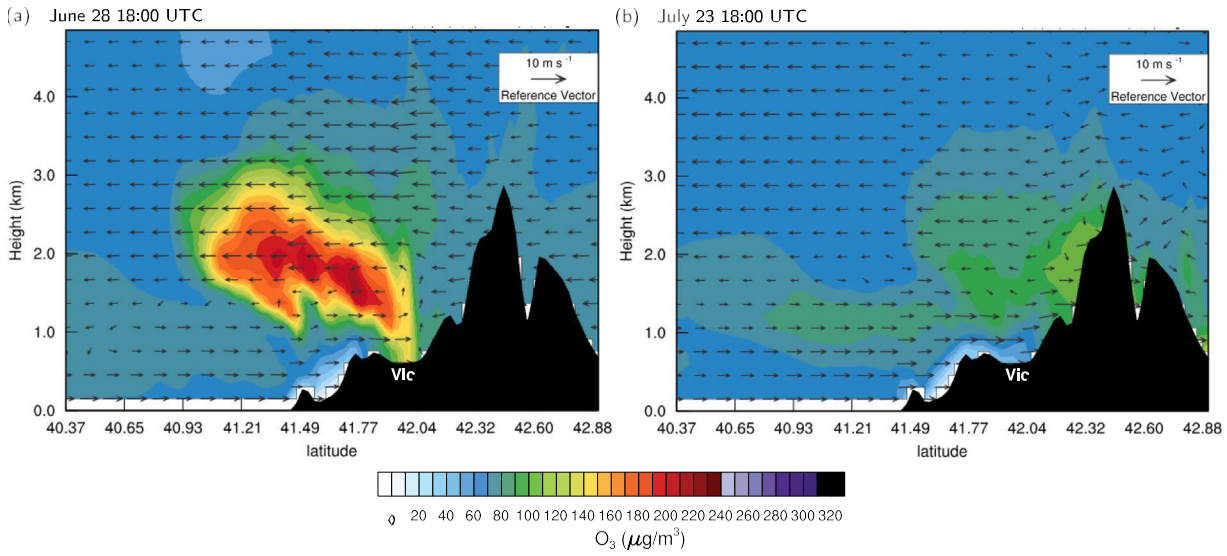

Fig. 9. Simulated ozone concentrations (shaded colors) and wind field vectors (black arrows) in south–north vertical cross sections marked in Fig. 8c and i. Maps shown correspond to June 28 at 18:00 UTC (a) and July 22 at 18:00 UTC (b). (For interpretation of the references to color in this figure legend, the reader is referred to the web version of this article.)

industrial emissions from the Barcelona harbor. However, the origin of this peak is not clearly defined because it took place later than other peaks located farther from the coast and it lasted 3 h, so it could also be caused by local emissions.

Along June 29 (Fig. 8e), model peak moved north-west of Barcelona following the Llobregat river pathway. In this case, observed peaks occurred later than forecasts, a feature seen above, and forecasts generally overestimated observations. Although maximum values in Llobregat valley evolved onshore with time following the sea breeze front, concentrations in AMB remained constantly high until late afternoon. These values by far exceeded the predicted ones at the coast. Yet, the peak extension towards the north was correctly forecast as illustrated by Bellver de Cerdanya station at 17 UTC (Fig. 8f). This successful forecast seems to be the result of the model correct sea breeze simulation and extension inland to carry pollutants to the Pyrenees. Otherwise, even though ARAMIS forecast ATE in Vic surroundings there were no exceedances registered there.

Differences in pollutants trajectory both days were mainly because of strong northerly winds in the north-east coasts blowing at morning hours of June 29 compared to southerlies observed there for June 28. During June 28, south-westerlies of the sea flow penetrated inland with sea breezes, thus, southerlies are observed all around the territory. In this scenario, flow motion moves generally through eastern Barcelona Besòs-Congost pathway. However, during June 29 early hours, northerlies blew along the north coast turning to north-easterlies with time. In this case, convergence with south-westerlies blowing along the south coast occurs in front of Barcelona and advects recirculated and newer pollutants through Llobregat pathway (Fig. 8e).

This type of comparative analysis has been performed for all days affected by the heat wave in Episode A (see Table 1). Circulation for June 30 has been found to be similar to June 29, through Llobregat pathway and driven by northerlies in the northern coast. In this case the only ITE occurred in Bellver de Cerdanya at 17 UTC (as for June 29) but according to ARAMIS simulation, ozone values exceeded the alert threshold in the affected area. However, for this day, there was no modeled plume over the sea so the main contribution was the advection from AMB, the VOCs emitted by the industries located in the valley, and probably also fumigation.

During Episode B, as shown in (Fig. 8g), ozone forecasts indicate morning peaks developed in Vic and Manresa surroundings and also high peaks in the north east, not supported by observations. The general circulation and flow advection for July 23 is similar to the first part of episode A (June 28). The main difference is that southerlies were stronger for July 23 and there were no northerlies blowing in the Pyrenees (Fig. 9b). Hence, winds along the coast had strong south components and air masses were transported north by flow motion in almost all territory (Fig. 8h). Even so, there were also easterlies in north-east of Catalonia due to breeze circulation perpendicular to the coast. Ozone high concentrations affected mainly Vic surroundings and the maximum was displaced inland with time. ARAMIS model also predicted high values a bit before they were measured and situated the maximum shifted slightly to the east of Vic. In this case, ozone also reached high values in the pre-Pyrenean station of Pardines at 16 UTC (Fig. 8i), located north from Manlleu, consistent with stronger northward fluxes during all day. Predicted ozone was lower than measured in the rest of the territory for most of daily hours and some wind components from AMB advected to Manresa and relative high concentrations were also measured there at 12:00 UTC (not shown).

All other days affected by the heatwave in episode B presented a similar behavior than that of July 23 when the strong southern advection affected stations located north of AMB. However, ATEs were only measured for July 23. Besides, July 22 and July 24 registered ITEs in Vic area and Montseny and also in some Llobregat valley stations. Additionally, the four stations affected in Episode B measured also ITEs on July 5, flow motion had the same pattern than Episode B but it was not in a heat wave period. Even so, in this period, model values were quite accurate.

Fig. 10 shows the results of the Integrated Process Rate (IPR) computed by CMAQ. For June 28 IPR analysis confirms the chemical formation of ozone in S. M. de Palautordera together with the ozone transport from layers above (Fig. 10a), while horizontal advection is increasing ozone in Montseny, probably transported from the latter station (Fig. 10b). In addition, fumigation is revealed to be the main process contributing to the exceedance registered in Gavà on June 29 (Fig. 10c) shown by the vertical diffusion dominance during the growth of the boundary layer. Instead, horizontal transport due to sea breeze is removing ozone in Gavà to inland stations such as Bellver de Cerdanya where ozone concentration increases when the sea breeze front reaches this location in late afternoon (Fig. 10d).

4.3. *HYSPLIT trajectory analysis*

Backward trajectories for selected stations computed with the HYSPLIT model are shown in Fig. 11. Interestingly, all stations which

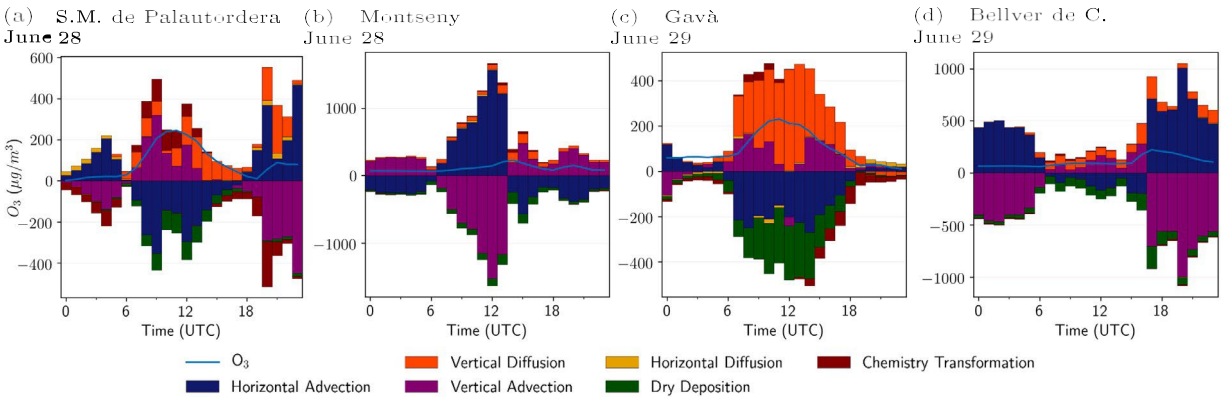

Fig. 10. Integrated Process Rate (IPR) analysis detailing the contributions at each time step in the tendency ozone concentration equation considering the following processes: horizontal and vertical advection, horizontal and vertical diffusion, dry deposition and chemical transformation. (For interpretation of the references to color in this figure legend, the reader is referred to the web version of this article.)

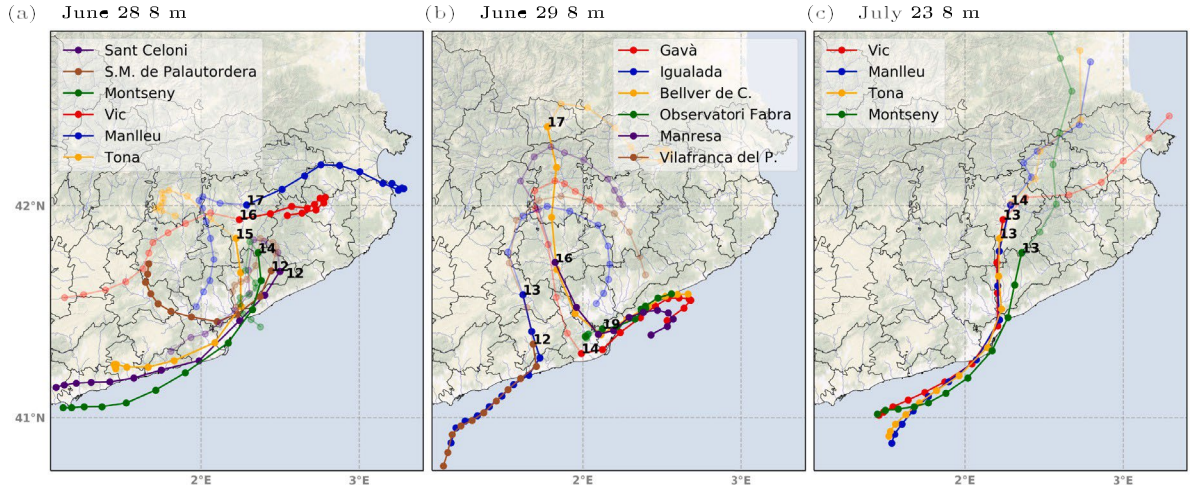

Fig. 11. Trajectories affecting selected XVPCA stations for June 28 (a), June 29 (b) and July 23 (c). Solid and semitransparent lines correspond to backward and forward trajectories, respectively. The number next to the station correspond to the UTC hour when both simulations started.

measured ATE present trajectories passing through AMB. For June 28, air from Barcelona took between 3 and 4 h to arrive to the affected stations, which means that NO_2 from morning traffic rush hours reached the stations at midday when sunlight was stronger. As it can be observed in Tona station trajectory, high values in Vic surroundings can also be attributed to precursors transport from Barcelona. However, trajectories in this location may not be very well estimated for peak hours. HYSPLIT uses WRF-ARW wind to generate trajectories, therefore if the real wind is not reproduced correctly neither will the trajectories. Previously explained hourly comparison allowed to see how southerly flow breezed inland and converged with easterly winds. However, wind observations show that northward breeze front penetrated further than model predicted and so did advection from AMB. For this particular moment, it was observed that modeled wind turned from easterlies to southerlies around Vic area later than the measured. Hence, to better estimate the trajectories ending at Tona, Vic and Manlleu, they were started one hour after the measured peak took place. Despite of this, trajectories in the northern stations still came from the east. As a result of this difference in wind direction between model and observations, ARAMIS underestimated values in Vic area. On the other hand, the observed westward advection could also bring pollutants from southern France or Italy (regional transport) to contribute to high ozone concentrations measured and modeled in the north-east coast.

Regarding the forward trajectories for June 28, a clear recirculation to the sea is observed in many stations. Trajectory in Montseny, the highest altitude station represented, shows that the air mass is over the sea in front of Barcelona 10 h later, consistent with the sea-breeze recirculation and storage in layers on the coast, a pattern previously explained ans shown in Fig. 9a.

For June 29, two different types of backward trajectories were described (Fig. 11b). The ones ending in Igualada and Vilafranca come from the sea in front of Tarragona, a highly industrialized area in the south coast of Catalonia. Pollutants may be advected over the sea from industries the day before, but given the concentrations measured then, the main contribution should be the mixing after convergence with flow coming from Barcelona coast. This air mixing is blocked at shoreline by an important massif but may result inland. On the other hand, air flow affecting Llobregat valley came, as expected, from above the sea in front of Barcelona. It passed through the capital driven by easterlies and headed north guided by Llobregat pathway. It took 6 h to the air flow to go from Barcelona to Bellver de Cerdanya. For Observatori Fabra station backward trajectory, which started at 19 UTC, air parcels are barely displaced remaining in Barcelona surroundings for most of the hours. This indicates that high Barcelona ozone concentrations along the afternoon may have the same origin as the advected inland and that local topography prevented part of the recirculated pollutants to disperse, rising concentrations in the capital. For this day, forward trajectories also indicate some kind of recirculation that can affect high values also measured for June 30.

During Episode B, trajectories also come from the city of Barcelona and they also took between 3 and 4 h to reach the measurement points. In contrast to June 28, in Episode B southerly breezes are

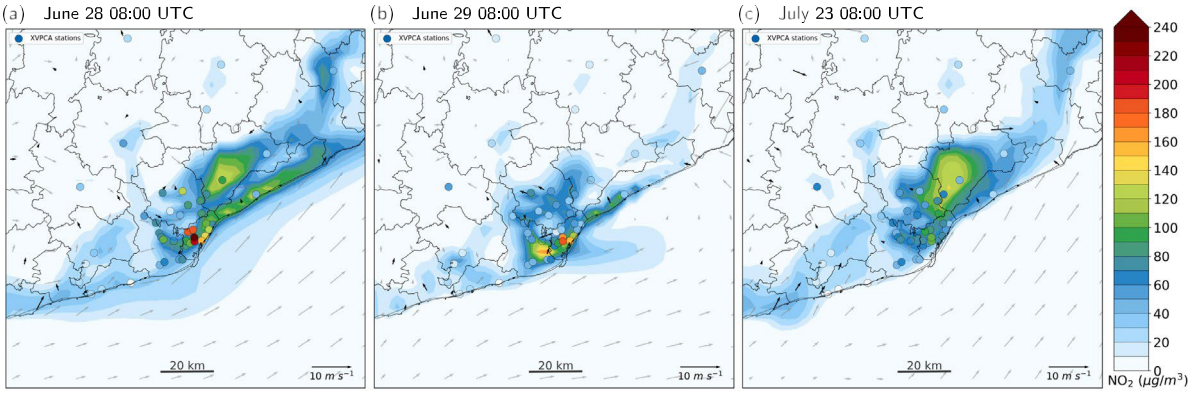

Fig. 12. Forecast (shaded colors) and observed NO_2 (solid circles) in Barcelona and surroundings for June 28 (a), June 29 (b) and July 23 (c) at 8 UTC.

stronger and advection is produced further north. Moreover, easterlies are weaker and vertical transport is not strong enough to recirculate pollutants (see Fig. 9b). Strong southerlies of bigger scales are the reason why recirculation is not observed, as it can be seen in forward trajectories heading north. As seen in Episode A, this plays a key role on high concentration episodes as an important recirculation after a high episode day may lead to ITEs in many areas the next day.

4.4. NO_2 *analysis*

Comparative maps of forecast and observed concentrations were also done for NO_2 so a comparison between both pollutants can give information about the chemistry involved (Fig. 12). Hourly NO_2 concentrations above 230 μg/m^3 were observed in Barcelona at morning hours of June 28 exceeding by far model forecasts. Consequently, and consistent with NO_x-limited regime previously explained, sub-urban stations downwind from Barcelona emissions record high O_3 concentrations due to NO_x advection. However, O_3 values measured in Barcelona stations were low. The next day, Saturday 29 of June, NO_2 in AMB at early hours were lower than the day before and this was better predicted by ARAMIS model. As expected in an urban VOCs-limited regime, ozone in Barcelona was high. Hence, this indicates that weekend effect also contributed to Episode A.

On the other hand, July 23 was a Thursday of a holiday period so NO_2 values were relatively low in AMB. In spite of that, ozone in Barcelona is also low and higher values are recorded inland. These differences suggest that the main contributing factor to high ozone values in Barcelona for June 29 is recirculation rather than emitted NO_2 influence. Moreover, although the advection for July 23 was from the AMB, the high ozone concentrations recorded inland for this day may not be so dependent on emissions in the AMB. The O_3 production in this case might be influenced by major biogenic VOCs emission in the area since these are usually higher in July than in June (Gómez and Baldasano, 1999) and as indicated by Gu et al. (2020) biogenic VOCs may be the main chemical-driver in heat waves ozone episodes. Hence, reducing AMB emissions will not probably lead to a significant reduction of the impact on human health for episodes similar to Episode B whilst for the first day of Episode A the reduction of these emissions will probably reduce the number of exceedances.

5. Conclusions

Two heat wave high ozone episodes were described for the summer of 2019 in Barcelona and surrounding region. Episode A took place between the 28th and 29th of June (4 ATEs and 1 ATE, respectively) and Episode B the 23rd of July (1 ATE). Both were characterized by high temperatures under heat wave conditions, and were driven by the sea breeze circulation in areas where the main ozone contribution was the advection of NO_x and VOCs from AMB and also its mixture with VOCs emitted by local sources. All combined with high temperatures and strong solar radiation enhanced ozone formation. Note that air temperatures during the episodes exceeded the threshold of 39 °C proposed in previous studies for the ozone suppression effect, which may lead to a plateau or even a decrease in ozone concentrations. However other particular local conditions described above such as recirculation from the sea may have played a role to compensate this, particularly in Episode A.

According to XVPCA measurements, the inland evolution of ozone peaks was through eastern Barcelona valleys (Besòs-Congost pathway) for June 28 and July 23 and through western valleys (Llobregat pathway) for June 29. These ozone peaks evolution are reproduced by the ARAMIS modeled O_3 values. The general tendency of ARAMIS forecasts is to overestimate the areas where the peak of O_3 concentrations occur and slightly underestimate O_3 concentrations in the rest of the territory. Another usual characteristic in modeled ozone is to increase O_3 concentrations a few hours before they are measured. In June 28, modeling results indicate hourly concentrations over 300 μg/m^3 in the north-east of the territory, a non-industrial area where unfortunately no measurement stations are available. This fact illustrates the benefit of increasing the observations in that area to improve the ozone pollution surveillance on the region. Additionally, modeled flows confirmed accumulation over the sea and recirculation in Episode A which may be the major reason for the big number of exceedances measured on June 29.

Trajectory analysis confirms the NO_x advection from AMB as a main cause of high ozone concentrations inland as almost all trajectories analyzed passed through this area several hours before reaching the stations with exceedances. Forward trajectories, process analysis and vertical cross sections also support the hypothesis of recirculation and accumulation of pollutants over the sea for June 28 and less intense for June 29 whilst no recirculation is observed for July 23.

Concerning the relation with NO_2, behaviors of NO_x-limited and VOCs-limited regimes are observed for June 28 in onshore regions and for June 29 in Barcelona, respectively, whilst for July 23 the relation is not clear but lead to conclude that for this day high ozone recorded inland is not so dependent on AMB precursor emissions. Results of this study not also contribute to a better understanding of mechanisms involved in heat-wave high O_3 episodes but also provide insight on potential measures to mitigate future events such as the different role of NO_2 precursors depending on the specific wind field circulation.

CRediT authorship contribution statement

Clara Jaén: Conceptualization, Methodology, Formal analysis Investigation, Data Curation, Writing - original draft, Visualization. **Mireia Udina:** Conceptualization, Data Curation, Writing - review & editing, Supervision. **Joan Bech:** Writing - review & editing, Supervision, Project administration.

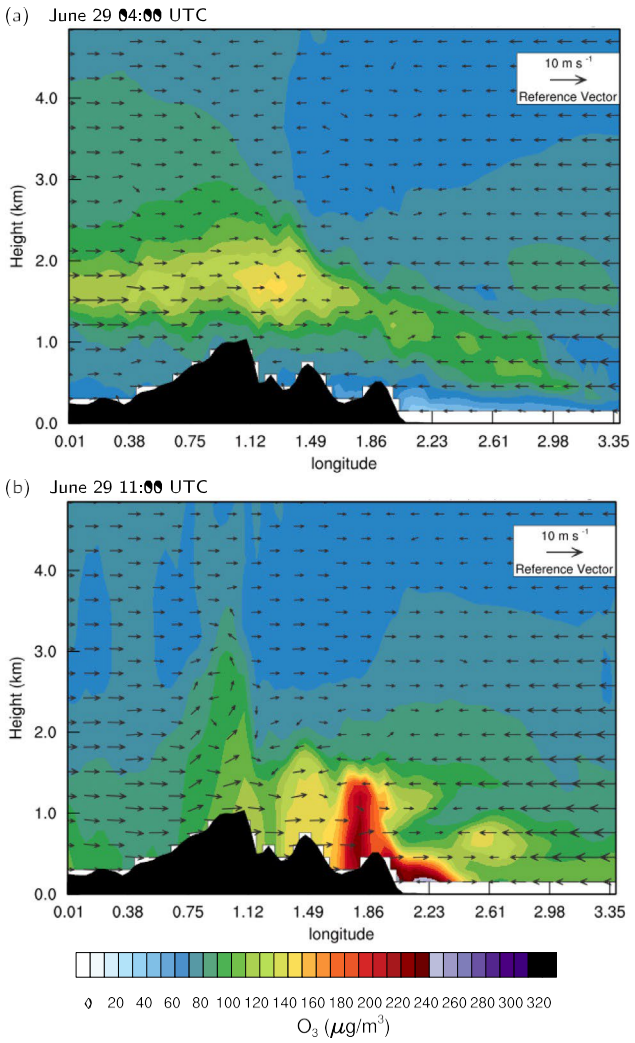

Fig. A.1. Simulated ozone concentrations (shaded colors) and wind field vectors (black arrows) in west-east vertical cross sections marked in Fig. 8d. Maps shown correspond to June 29 at 04:00 UTC (a) and June 29 at 11:00 UTC (b).

Declaration of competing interest

The authors declare that they have no known competing financial interests or personal relationships that could have appeared to influence the work reported in this paper.

Acknowledgments

Support for this study was provided by Master+UB program (University of Barcelona, Spain) and from grant RTI2018-098693-B-C32 (AEI). Authors are very grateful to Territory and Sustainability Department for the measurement data of XVPCA stations, to the Meteorological Service of Catalonia for the meteorological data and to Copernicus Climate Change Service for reanalysis data. And finally, thanks to Carmen Aguirre from the UNAM university and Miguel Garcia from University of Barcelona for their help.

Appendix A. Complementary figures

This appendix provides additional cross sections of ozone concentrations and wind fields. In particular, Fig. A.1 displays cross sections modeled for the 29 June Episode at 04:00 and 11:00 UTC.

Table B.1
Contingency table.

		Observed	
		Yes	No
Simulated	Yes	Hits	False alarms
	No	Misses	Correct negatives

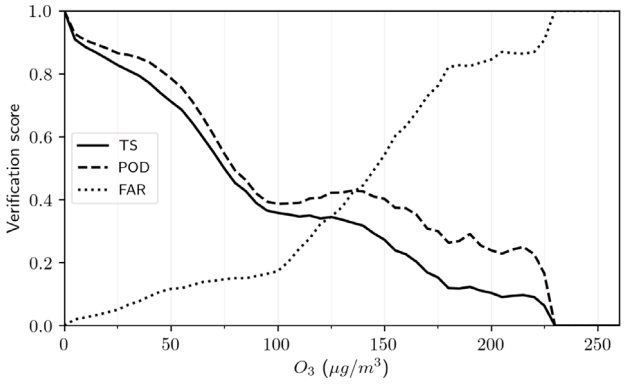

Fig. B.1. Verification scores for different ozone concentration thresholds including probability of detection (POD), false alarm ratio (FAR) and threat score (TS) for all stations during both episodes.

Appendix B. Contingency tables

As indicated by Wilks (2011) and WWRP/WGNE (2015) particular aspects of forecast performance can be described by categorical statistics computed from the elements in a contingency table (Table B.1). Namely, threat score (TS), probability of detection (POD) and false alarm ratio (FAR) as follows:

$$TS = \frac{hits}{hits + false\ alarms + misses} \quad (5)$$

$$POD = \frac{hits}{hits + misses} \quad (6)$$

$$FAR = \frac{false\ alarms}{hits + false\ alarms} \quad (7)$$

where a perfect score is given by TS = 1, POD = 1 and FAR = 0. Fig. B.1 shows an evaluation of ozone forecasts considering different concentrations for the two Episodes studied.

References

Anenberg, S.C., Horowitz, L.W., Tong, D.Q., West, J.J., 2010. An estimate of the global burden of anthropogenic ozone and fine particulate matter on premature human mortality using atmospheric modeling. Environ. Health Perspect. 118 (9), 1189–1195.

Arasa, R., Soler, M.R., Olid, M., 2012. Evaluating the performance of a regional-scale photochemical modelling system: Part I. Ozone predictions. Int. Sch. Res. Notices 2012, 1–22.

Arnold, S., Lombardozzi, D., Lamarque, J.-F., Richardson, T., Emmons, L., Tilmes, S., Sitch, S., Folberth, G., Hollaway, M., Val Martin, M., 2018. Simulated global climate response to tropospheric ozone-induced changes in plant transpiration. Geophys. Res. Lett. 45 (23), 13070–13079.

Byun, D.W., Ching, J., et al., 1999. Science Algorithms of the EPA Models-3 Community Multiscale Air Quality (CMAQ) Modeling System. US Environmental Protection Agency, Office of Research and Development Washington, DC, USA.

Camalier, L., Cox, W., Dolwick, P., 2007. The effects of meteorology on ozone in urban areas and their use in assessing ozone trends. Atmos. Environ. 41 (33), 7127–7137.

Carnerero, C., Pérez, N., Petäjä, T., Laurila, T.M., Ahonen, L.R., Kontkanen, J., Ahn, K.-H., Alastuey, A., Querol, X., 2019. Relating high ozone, ultrafine particles, and new particle formation episodes using cluster analysis. Atmos. Environ.: X 4, 100051.

Chameides, W., Walker, J.C., 1973. A photochemical theory of tropospheric ozone. J. Geophys. Res. 78 (36), 8751–8760.
Chen, F., Dudhia, J., 2001. Coupling an advanced land surface-hydrology model with the penn state-NCAR MM5 modeling system. Part I: Model implementation and sensitivity. Mon. Weather Rev. 129 (4), 569–585.
Chen, P.-Y., Tan, P.-H., Chou, C.C.-K., Lin, Y.-S., Chen, W.-N., Shiu, C.-J., 2019. Impacts of holiday characteristics and number of vacation days on ''holiday effect'' in Taipei: Implications on ozone control strategies. Atmos. Environ. 202, 357–369.
Colette, A., Andersson, C., Baklanov, A., Bessagnet, B., Brandt, J., Christensen, J.H., Doherty, R., Engardt, M., Geels, C., Giannakopoulos, C., Hedegaard, G.B., Katragkou, E., Langner, J., Lei, H., Manders, A., Melas, D., Meleux, F., Rouïl, L., Sofiev, M., Soares, J., Stevenson, D.S., Tombrou-Tzella, M., Varotsos, K.V., Young, P., 2015. Is the ozone climate penalty robust in Europe? Environ. Res. Lett. 10 (8), 084015.
Corsmeier, U., Kalthoff, N., Kolle, O., Kotzian, M., Fiedler, F., 1997. Ozone concentration jump in the stable nocturnal boundary layer during a LLJ-event. Atmos. Environ. 31 (13), 1977–1989.
Crutzen, P., 1973. A discussion of the chemistry of some minor constituents in the stratosphere and troposphere. Pure Appl. Geophys. 106 (1), 1385–1399.
Dear, K., Ranmuthugala, G., Kjellström, T., Skinner, C., Hanigan, I., 2005. Effects of temperature and ozone on daily mortality during the august 2003 heat wave in France. Arch. Environ. Occup. Health 60 (4), 205–212.
Dudhia, J., 1989. Numerical study of convection observed during the winter monsoon experiment using a mesoscale two-dimensional model. J. Atmos. Sci. 46 (20), 3077–3107.
Elansky, N., Shilkin, A., Ponomarev, N., Semutnikova, E., Zakharova, P., 2020. Weekly patterns and weekend effects of air pollution in the moscow megacity. Atmos. Environ. 224, 117303.
Filleul, L., Cassadou, S., Médina, S., Fabres, P., Lefranc, A., Eilstein, D., Le Tertre, A., Pascal, L., Chardon, B., Blanchard, M., et al., 2006. The relation between temperature, ozone, and mortality in nine french cities during the heat wave of 2003. Environ. Health Perspect. 114 (9), 1344–1347.
Francis, X., Chemel, C., Sokhi, R., Norton, E., Ricketts, H., Fisher, B., 2011. Mechanisms responsible for the build-up of ozone over South East England during the august 2003 heatwave. Atmos. Environ. 45 (38), 6880–6890.
Gangoiti, G., Millán, M.M., Salvador, R., Mantilla, E., 2001. Long-range transport and re-circulation of pollutants in the western mediterranean during the project regional cycles of air pollution in the west-central mediterranean area. Atmos. Environ. 35 (36), 6267–6276.
Gómez, O., Baldasano, J., 1999. Biogenic VOC emission inventory for Catalonia, Spain. WIT Trans. Ecol. Environ. 36, 1–7.
Gonçalves, M., Jiménez-Guerrero, P., Baldasano, J.M., 2009. Contribution of atmospheric processes affecting the dynamics of air pollution in South-Western Europe during a typical summertime photochemical episode. Atmos. Chem. Phys. 9 (3), 849–864.
Grell, G.A., Dévényi, D., 2002. A generalized approach to parameterizing convection combining ensemble and data assimilation techniques. Geophys. Res. Lett. 29 (14), 38–1–38–4.
Gu, Y., Li, K., Xu, J., Liao, H., Zhou, G., 2020. Observed dependence of surface ozone on increasing temperature in Shanghai, China. Atmos. Environ. 221, 117108.
Heuss, J.M., Kahlbaum, D.F., Wolff, G.T., 2003. Weekday/weekend ozone differences: what can we learn from them? J. Air Waste Manage. Assoc. 53 (7), 772–788.
Hong, S.-Y., Noh, Y., Dudhia, J., 2006. A new vertical diffusion package with an explicit treatment of entrainment processes. Mon. Weather Rev. 134 (9), 2318–2341.
Hu, X.-M., Klein, P.M., Xue, M., Zhang, F., Doughty, D.C., Forkel, R., Joseph, E., Fuentes, J.D., 2013. Impact of the vertical mixing induced by low-level jets on boundary layer ozone concentration. Atmos. Environ. 70, 123–130.
Jacob, D.J., Winner, D.A., 2009. Effect of climate change on air quality. Atmos. Environ. 43 (1), 51–63.
Lee, J.Y., Lee, S.H., Hong, S.-C., Kim, H., 2017. Projecting future summer mortality due to ambient ozone concentration and temperature changes. Atmos. Environ. 156, 88–94.
Lee, J.D., Lewis, A.C., Monks, P.S., Jacob, M., Hamilton, J.F., Hopkins, J.R., Watson, N.M., Saxton, J.E., Ennis, C., Carpenter, L.J., et al., 2006. Ozone photochemistry and elevated isoprene during the UK heatwave of august 2003. Atmos. Environ. 40 (39), 7598–7613.
Li, L., Chen, C., Huang, C., Huang, H., Zhang, G., Wang, Y., Wang, H., Lou, S., Qiao, L., Zhou, M., et al., 2012. Process analysis of regional ozone formation over the Yangtze River Delta, China using the community multi-scale air quality modeling system. Atmos. Chem. Phys. 12 (22), 10971.
Liu, X.-H., Zhang, Y., Xing, J., Zhang, Q., Wang, K., Streets, D.G., Jang, C., Wang, W.-X., Hao, J.-M., 2010. Understanding of regional air pollution over China using CMAQ, part II. Process analysis and sensitivity of ozone and particulate matter to precursor emissions. Atmos. Environ. 44 (30), 3719–3727.
Massagué, J., Carnerero, C., Escudero, M., Baldasano, J.M., Alastuey, A., Querol, X., 2019. 2005-2017 ozone trends and potential benefits of local measures as deduced from air quality measurements in the north of the Barcelona metropolitan area. Atmos. Chem. Phys. 19 (11), 7445–7465.
Meehl, G.A., Tebaldi, C., Tilmes, S., Lamarque, J.-F., Bates, S., Pendergrass, A., Lombardozzi, D., 2018. Future heat waves and surface ozone. Environ. Res. Lett. 13 (6), 064004.
Meteocat, 2019a. Butlletí climàtic mensual. juliol del 2019. https://static-m.meteo.cat/wordpressweb/wp-content/uploads/2019/08/21073719/Butlletí-Juliol2019.pdf, Last accessed on 2020-07-22.
Meteocat, 2019b. Butlletí climàtic mensual. juny del 2019. https://static-m.meteo.cat/wordpressweb/wp-content/uploads/2019/07/23104303/Butlletí-Juny2019.pdf, Last accessed on 2020-07-22.
Millán, M.M., Mantilla, E., Salvador, R., Carratalá, A., Sanz, M.J., Alonso, L., Gangoiti, G., Navazo, M., 2000. Ozone cycles in the western Mediterranean basin: interpretation of monitoring data in complex coastal terrain. J. Appl. Meteorol. 39 (4), 487–508.
Millán, M., Salvador, R., Mantilla, E., Artnano, B., 1996. Meteorology and photochemical air pollution in southern Europe: experimental results from EC research projects. Atmos. Environ. 30 (12), 1909–1924.
Millán, M., Salvador, R., Mantilla, E., Kallos, G., 1997. Photooxidant dynamics in the mediterranean basin in summer: Results from European research projects. J. Geophys. Res.: Atmos. 102 (D7), 8811–8823.
Mlawer, E.J., Taubman, S.J., Brown, P.D., Iacono, M.J., Clough, S.A., 1997. Radiative transfer for inhomogeneous atmospheres: RRTM, a validated correlated-k model for the longwave. J. Geophys. Res. 102 (D14), 16663–16682.
Monin, A., Obukhov, A., 1954. Basic laws of turbulent mixing in the surface layer of the atmosphere. Contrib. Geophys. Inst. Acad. Sci. USSR 151, 163–187.
Ortega, S., Soler, M., Alarcón, M., Arasa, R., 2009. MNEQA, an emissions model for photochemical simulations. Atmos. Environ. 43 (24), 3670–3681.
Pleim, J.E., Chang, J.S., 1992. A non-local closure model for vertical mixing in the convective boundary layer. Atmos. Environ. A 26 (6), 965–981.
Pu, X., Wang, T., Huang, X., Melas, D., Zanis, P., Papanastasiou, D., Poupkou, A., 2017. Enhanced surface ozone during the heat wave of 2013 in yangtze river Delta region, China. Sci. Total Environ. 603, 807–816.
Pusede, S.E., Steiner, A.L., Cohen, R.C., 2015. Temperature and recent trends in the chemistry of continental surface ozone. Chem. Rev. 115 (10), 3898–3918.
Pyrgou, A., Hadjinicolaou, P., Santamouris, M., 2018. Enhanced near-surface ozone under heatwave conditions in a Mediterranean island. Sci. Rep. 8 (1), 9191.
Qin, Y., Tonnesen, G., Wang, Z., 2004. Weekend/weekday differences of ozone, NOx, CO, VOCs, PM10 and the light scatter during ozone season in southern California. Atmos. Environ. 38 (19), 3069–3087.
Querol, X., Gangoiti, G., Mantilla, E., Alastuey, A., Minguillón, M., Amato, F., Reche, C., Viana, M., Moreno, T., Karanasiou, A., et al., 2017. Phenomenology of high-ozone episodes in NE Spain. Atmos. Chem. Phys. 17 (4), 2817–2838.
Querol, X., Mantilla, E., Ruiz, C.R., Lopez-Soler, A., Juan, R., et al., 1998. Seasonal evolution of suspended particles around a large coal-fired power station: Chemical characterization. Atmos. Environ. 32 (4), 719–731.
Racherla, P.N., Adams, P.J., 2006. Sensitivity of global tropospheric ozone and fine particulate matter concentrations to climate change. J. Geophys. Res.: Atmos. 111 (D24).
Schnell, J.L., Prather, M.J., 2017. Co-occurrence of extremes in surface ozone, particulate matter, and temperature over eastern North America. Proc. Natl. Acad. Sci. 114 (11), 2854–2859.
Shen, L., Mickley, L.J., Gilleland, E., 2016. Impact of increasing heat waves on US ozone episodes in the 2050s: Results from a multimodel analysis using extreme value theory. Geophys. Res. Lett. 43 (8), 4017–4025.
Sillman, S., He, D., 2002. Some theoretical results concerning O3-NOx-VOC chemistry and NOx-VOC indicators. J. Geophys. Res.: Atmos. 107 (D22), ACH–26.
Sillman, S., Logan, J.A., Wofsy, S.C., 1990. The sensitivity of ozone to nitrogen oxides and hydrocarbons in regional ozone episodes. J. Geophys. Res.: Atmos. 95 (D2), 1837–1851.
Skamarock, W.C., Klemp, J., Dudhia, J., Gill, D., Barker, D., Wang, W., Powers, J., 2008. A Description of the Advanced Research WRF Version 3. NCAR Tech Notes-475+ STR, National Center for Atmospheric Research (NCAR).
Soler, M., Arasa, R., Merino, M., Olid, M., Ortega, S., 2011. Modelling local sea-breeze flow and associated dispersion patterns over a coastal area in north-east Spain: a case study. Bound.-Layer Meteorol. 140 (1), 37–56.
Soler, M.R., Gamez, P., Olid, M., 2015. Aramis a regional air quality model for air pollution management: evaluation and validation. Fis. Tierra 27, 113–138.
Souri, A.H., Nowlan, C.R., Wolfe, G.M., Lamsal, L.N., Miller, C.E.C., Abad, G.G., Janz, S.J., Fried, A., Blake, D.R., Weinheimer, A.J., et al., 2020. Revisiting the effectiveness of HCHO/NO2 ratios for inferring ozone sensitivity to its precursors using high resolution airborne remote sensing observations in a high ozone episode during the KORUS-AQ campaign. Atmos. Environ. 224, 117341.
Stathopoulou, E., Mihalakakou, G., Santamouris, M., Bagiorgas, H., 2008. On the impact of temperature on tropospheric ozone concentration levels in urban environments. J. Earth Syst. Sci. 117 (3), 227–236.
Stein, A., Draxler, R.R., Rolph, G.D., Stunder, B.J., Cohen, M., Ngan, F., 2015. NOAA's HYSPLIT atmospheric transport and dispersion modeling system. Bull. Am. Meteorol. Soc. 96 (12), 2059–2077.
Steiner, A.L., Davis, A.J., Sillman, S., Owen, R.C., Michalak, A.M., Fiore, A.M., 2010. Observed suppression of ozone formation at extremely high temperatures due to chemical and biophysical feedbacks. Proc. Natl. Acad. Sci. 107 (46), 19685–19690.
Stevenson, D., Doherty, R., Sanderson, M., Johnson, C., Collins, B., Derwent, D., 2005. Impacts of climate change and variability on tropospheric ozone and its precursors. Faraday Discuss. 130, 41–57.

Thompson, G., Rasmussen, R.M., Manning, K., 2004. Explicit forecasts of winter precipitation using an improved bulk microphysics scheme. Part I: Description and sensitivity analysis. Mon. Weather Rev. 132 (2), 519–542.

Toll, I., Baldasano, J., 2000. Modeling of photochemical air pollution in the Barcelona area with highly disaggregated anthropogenic and biogenic emissions. Atmos. Environ. 34 (19), 3069–3084.

Trapero, L., Bech, J., Duffourg, F., Esteban, P., Lorente, J., 2013. Mesoscale numerical analysis of the historical november 1982 heavy precipitation event over andorra (eastern pyrenees). Nat. Hazards Earth Syst. Sci. 13, 2969–2990.

Udina, M., Soler, M.R., Olid, M., Jiménez-Esteve, B., Bech, J., 2020. Pollutant vertical mixing in the nocturnal boundary layer enhanced by density currents and low-level jets: two representative case studies. Bound.-Lay. Meteorol. 174 (2), 203–230.

Valverde, V., Pay, M.T., Baldasano, J.M., 2016. Ozone attributed to madrid and barcelona on-road transport emissions: Characterization of plume dynamics over the Iberian Peninsula. Sci. Total Environ. 543, 670–682.

Wei, D., Fuentes, J.D., Gerken, T., Trowbridge, A.M., Stoy, P.C., Chamecki, M., 2019a. Influences of nitrogen oxides and isoprene on ozone-temperature relationships in the Amazon rain forest. Atmos. Environ. 206, 280–292.

Wei, W., Li, Y., Ren, Y., Cheng, S., Han, L., 2019b. Sensitivity of summer ozone to precursor emission change over Beijing during 2010–2015: A WRF-Chem modeling study. Atmos. Environ. 218, 116984.

WHO, et al., 2006. WHO Air Quality Guidelines for Particulate Matter, Ozone, Nitrogen Dioxide and Sulfur Dioxide: Global Update 2005: Summary of Risk Assessment. Technical Report, World Health Organization.

Wilks, D.S., 2011. Statistical Methods in the Atmospheric Sciences, Vol. 100. Academic press.

Williams, S., Nitschke, M., Sullivan, T., Tucker, G.R., Weinstein, P., Pisaniello, D.L., Parton, K.A., Bi, P., 2012. Heat and health in Adelaide, South Australia: assessment of heat thresholds and temperature relationships. Sci. Total Environ. 414, 126–133.

WWRP/WGNE, 2015. Forecast verification methods across time and space scales. https://www.cawcr.gov.au/projects/verification/, Last accessed on 2020-10-02.

Yarwood, G., Rao, S., Yocke, M., Whitten, G., 2005. Updates to the carbon bond chemical mechanism: CB05. In: Final Report to the US EPA, RT-0400675, Vol. 8.

Yu, D., Tan, Z., Lu, K., Ma, X., Li, X., Chen, S., Zhu, B., Lin, L., Li, Y., Qiu, P., et al., 2020. An explicit study of local ozone budget and NOx-VOCs sensitivity in shenzhen China. Atmos. Environ. 224, 117304.

Zhang, Q., Xue, D., Liu, X., Gong, X., Gao, H., 2019. Process analysis of PM2. 5 pollution events in a coastal city of China using CMAQ. J. Environ. Sci. 79, 225–238.

Zhao, K., Bao, Y., Huang, J., Wu, Y., Moshary, F., Arend, M., Wang, Y., Lee, X., 2019. A high-resolution modeling study of a heat wave-driven ozone exceedance event in New York city and surrounding regions. Atmos. Environ. 199, 368–379.